Observation operator and detection limits for MODIS and VIIRS Fire Radiative Power products

Mikhail Sofiev, Rostislav Kouznetsov

Finnish Meteorological Institute, Erik Palmenin Aukio 1, Helsinki, Finland, mikhail.sofiev@fmi.fi

Abstract

We analyze the MODIS and VIIRS active-fire Fire Radiative Power (FRP) products and suggest an approximation for the FRP detection limit as a linear function of a pixel area and develop analytical observation operators for both pixel-level and gridded FRP products. We have shown that the collection-6.1 of MODIS has the FRP detection limit at 3.7 MW in case of a nadir retrieval at a clear-sky night. For a daytime sideview, it reaches as high as 40 MW. For VIIRS, the smallest fire reliably detected at night is 0.5 MW. Application of the developed operators for the cross mapping the MODIS and VIIRS datasets at the pixel/granule level confirmed their consistency. Applying the grid-level operators alongside satellite overpass and weather data, we generated global maps of fire detection probabilities, revealing regional variations. As a global average, probability of detection of powerful fires is 78% for MODIS (88% for VIIRS). Variations between regions are large: in some equatorial areas this probability is less than 30% for MODIS (40% for VIIRS).

Key words: Fire Radiative Power, MODIS, VIIRS, observation operator, sensitivity, detection limit

1. Introduction

Vegetation fires have long been recognized as one of the most-powerful phenomena affecting the lifecycle of forest and grassland ecosystems, a strong source of atmospheric pollutants, and a significant climate factor (Crutzen et al., 1979; Kollanus et al., 2017; Buchholz et al., 2022; Khabarov et al., 2016; Chowdhury et al., 2025). Since fires are a global phenomenon, satellite observations are the natural way of their systematic monitoring. Two types of products are the most-important in this respect: burnt-area scars left by recently occurred fires (Chuvieco et al., 2019) and active-fire products, such as Fire Radiative Power (FRP) and Temperature Anomaly (TA), which rely on a thermal fingerprint of active fires (Ichoku and Kaufman, 2005; Kaiser et al., 2012; Kaufman et al., 1998; Parrington et al., 2025). Both types of products have their strong and weak points (Archibald and Roy, 2009; Roy et al., 2008; Schroeder et al., 2014a; Vilar et al., 2015; Zubkova et al., 2023). This work concentrates on active-fire products.

Observations of active fires produce two types of data: hot spot counts (Arino et al., 2012; Li et al., 2001) and fire radiative power FRP (Kaufman et al., 1998; Ichoku and Kaufman, 2005; Schroeder et al., 2014b; Giglio et al., 2016, 2021; Schroeder, 2020a, 2020b; Xu and Wooster, 2023). The key strength of the FRP - based approach is that the data characterizes the fire intensity at the moment of the observations. It allows to construct operational global fire information systems (Kaiser et al., 2012; Wiedinmyer et al., 2011; Sofiev et al., 2009; Chen et al., 2022), build injection-height models (Freitas et al., 2007; Sofiev et al., 2013, 2012; Rémy et al., 2017; Li et al., 2022), and estimate characteristic diurnal cycle of the fire activity (Soares et al., 2015; Sofiev et al., 2013).

A limitation of the active-fire data is a tendency to miss a substantial fraction of fires – a so-called omission error. Thus, Schroeder et al. (2008) used Advanced Spaceborne Thermal Emission and Reflection Radiometer (ASTER) and the Landsat 7 Enhanced Thematic Mapper Plus (ETM+) at 30 m spatial resolution to provide a “ground truth” dataset for the MODIS algorithm. They produced summary

statistics indicating that 50 to 100 ASTER fire pixels (corresponding to 5%-10% of area of a 1 km pixel) are necessary to trigger the MODIS fire detection with >80% probability. The uncertainty in the estimate was associated with the fraction of the pixel area covered by trees. No quantitative estimation of the FRP detection limit was provided.

A fire can be missed if its radiative power is below the detection limit of a given instrument/algorithm. This threshold, in turn, depends on the overall contrast of the scene, i.e., the size of the burning area, the size of the pixel, background temperature of non-burning areas around the burning pixel. A larger pixel means stronger averaging and lower contrast. We are aware of only one study so far that quantified the dependence of the minimum strength of the observable fire on the pixel size (Maier et al., 2013), which considered MODIS Collection 5 for Australia.

Among the key reasons for omission error of low-orbit satellites is a cloud obscuration during the satellite overpass. This error is milder for geostationary-based instruments, such as SEVIRI, GOES, and HIMAWARI (Roberts and Wooster, 2008; Schroeder et al., 2007; Schultz et al., 2008; Xu et al., 2017) because they can provide information for a specific location several times per hour, thus avoiding some clouds. However, the problem still exists: the effect of cloud obscuration was studied for Brazilian Amazon (Schroeder et al., 2007) showing the GOES omission error of 11% of fire counts during the considered episode.

Utilization of any observational data in numerical models requires a procedure that relates the observed quantities and the ones computed by the model. It has been shown (Bocquet et al., 2015) that the model-measurement comparison should be performed in the observational space, i.e., the modelled quantities should be converted to the observed ones using an Observation Operator, hereinafter OOp (Bocquet et al., 2015; Carrassi et al., 2018). In principle, every type of observation requires its own OOp, but in many cases the modelled quantities are considered to be close enough to the observed ones for

assuming the identity OOp. For satellite data, this is practically never the case, therefore sophisticated operators have been developed targeting radiance as one of the primary remote-sensing variables (Evans, 2007; Greenwald et al., 2004, 2002; Kostka et al., 2014). Such operators involve radiative transfer models and provide a sufficiently accurate mapping of the model data to variables observed by the satellite instrument. It is also possible to construct simpler operators converting the model output to an intermediate remote-sensing variable, which is deemed accurate. For instance, (Banks et al., 2012) developed an OOp for the remote-sensing ocean color synthetic measurement at the water surface, whereas the key step in the OOp for OMI NO_2 column data is accounting for the instrument averaging kernel (Boersma et al., 2011).

For the FRP data, an identity operator has been used till today (Kaiser et al., 2012), and we are not aware of any non-trivial OOp developed for the FRP retrievals.

The objectives of the current work are: (i) to quantify the detection limit of individual MODIS (collection 6.1) and VIIRS (collections 2 and 2.1) retrievals of FRP and to suggest a unified analytical approximation as a function of pixel size; (ii) to suggest an observation operator for gridded MODIS and VIIRS FRP products; (iii) to apply the developed OOp to quantify the omission error over the globe and estimate the probability of fire detection by MODIS and VIIRS during the fire season as a function of the location, (iv) to demonstrate the OOp application to mapping the level-2 MODIS and VIIRS FRP products.

The paper is organized as follows. The next section 2 describes the input data of the assessment, section 3 introduces the study methodology, derives the sensitivity of the FRP products, detection limit, and OOp formulations; section 4 presents the results of the OOp application: global maps of the MODIS and VIIRS omission error and application of pixel-level OOp to cross-mapping the MODIS and VIIRS pixel-/granule-level FRP retrievals. These results are discussed in section 5.

2. Input data

2.1. MODIS Fire Radiative Power and supplementary products

The MODIS dataset used in this study consists of the level-2 (L2) Fire Radiative Power retrievals MOD14 and MYD14 from the instrument onboard Terra (2000-2023) and Aqua (2002-2023) satellites respectively. Hereinafter, the common notation will be MxD14. The L2 products were downloaded from Atmosphere Archive & Distribution System (LAADS) Distributed Active Archive Center (DAAC) (https://ladsweb.nascom.nasa.gov/, visited 12.10.2025, (Giglio and Justice, 2021a, 2021b). The data after 2023 were not used to avoid impact of the TERRA constellation exit maneuvers.

The MODIS L2 products are organized in granules, i.e., chunks of data collected during 5 minute intervals. Each MxD14 granule contains a field of flags for every pixel in a granule indicating if a detection was possible or not (cloud obscuration, failed retrieval, sun glint, water surface etc.) and a list of overheated pixels with FRP, geolocation, position in the swath, pixel size, etc. The geolocation of non-overheated pixels was picked from the MODIS cloud products MxD35 collection 6.1 (MODIS Atmosphere Science Team, 2017a, 2017b).

The key variables used in the assessment are: (i) the pixel-wise FRP expressed in megawatts throughout the paper; (ii) quality flags of MxD14, (iii) geolocation information of individual pixels of MxD35.

The FRP retrievals were censored by removing ~0.6% of pixels with unphysically strong FRP, $P_p > 500\ MW$. Secondly, the first months of MODIS Terra operations, until November 2000, were removed entirely due to known problems with the sensor (Giglio et al., 2021). No other filtering was applied.

2.2. VIIRS Fire Radiative Power products

The VIIRS data from the instruments onboard SUOMI-NPP (2012-2024) and NOAA-20 (2018-2024) satellites were obtained from the same NASA LAADS DAAC Earth Data server as the MODIS products.

We used VNP14IMG and VJ114IMG (Giglio, 2024a, 2024b) for FRP, locations of detected overheated pixels, and the detection mask, and VNP03IMG and VJ103IMG products (VIIRS Calibration Support Team (VCST), 2021a, 2021b) for pixel geolocation. The corresponding common notations hereinafter are Vxx14 and Vxx03. Data before February 2012 were discarded to avoid suspiciously large number of fires reported in the first days of the instrument operation. No other filtering was applied.

3. Methodology

3.1. Size of a MODIS and VIIRS pixel

An approximate formula for the pixel size calculations for both MODIS and VIIRS has been suggested by Ichoku and Kaufman (2005) with a reference to Masahiro Nishihama (pers. comm. 2004) and the MODIS Algorithm Technical Basis Document ATBD (Nishihama et al., 1997). A ground pixel size along the scan ΔS and the satellite track ΔT directions are functions of the scanning angle θ and orbit parameters:

$$\Delta S = R_e s \left[\frac{cos\theta}{\sqrt{(R_e/r)^2 - sin^2\theta}} - 1 \right] \quad (1)$$

$$\Delta T = rs \left[cos\theta - \sqrt{(R_e/r)^2 - sin^2\theta} \right] \quad (2)$$

where R_e=6378.137 km is radius of Earth, $r=R_e+h$, h is altitude of the orbit (705 km for MODIS), p is pixel nadir size (1 km for MODIS), $s=p/h$=0.0014184397 (MODIS), and scanning angle θ is determined by the pixel number *i* in the scan line consisting for MODIS of totally $N=2030$ pixels:

$$\theta_i = s\left(i - \frac{N+1}{2}\right) \quad (3)$$

These formulas can also be applied to VIIRS with h=825.2 km, $N=6400$ non-aggregated pixels, s=0.375 km (Schroeder et al., 2014b; Wolfe et al., 2013). Accuracy of this approximation has been verified

against the instrument look-up table (W. Schroeder, pers.comm., 2022) and showed the error not exceeding 0.2% for all variables of (1) – (3).

3.2. Swath geometry

Formulas (1) – (3) are illustrated in Figure 1 for MODIS and Figure 2 for VIIRS. The total width of the MODIS scan over the Earth surface is ~2063 km, and the pixel area varies from 1 km^2 in nadir view at θ= 0 up to 9.66 km^2 at the edge of the swath at θ= 55° (Figure 1 a). About 40% of the swath is covered by pixels with A_p < 2 km^2 and only 20% - by pixels with A_p > 6 km^2 (Figure 1 b,c). MODIS swath has 10 detectors in the track direction (Nishihama et al., 1997). The growing size of the pixels towards the edge of the swath means that the neighboring swaths partly overlap along the track direction (Figure 1 d, see also Figure 3-1 of Nishihama et al. (1997) for MODIS).

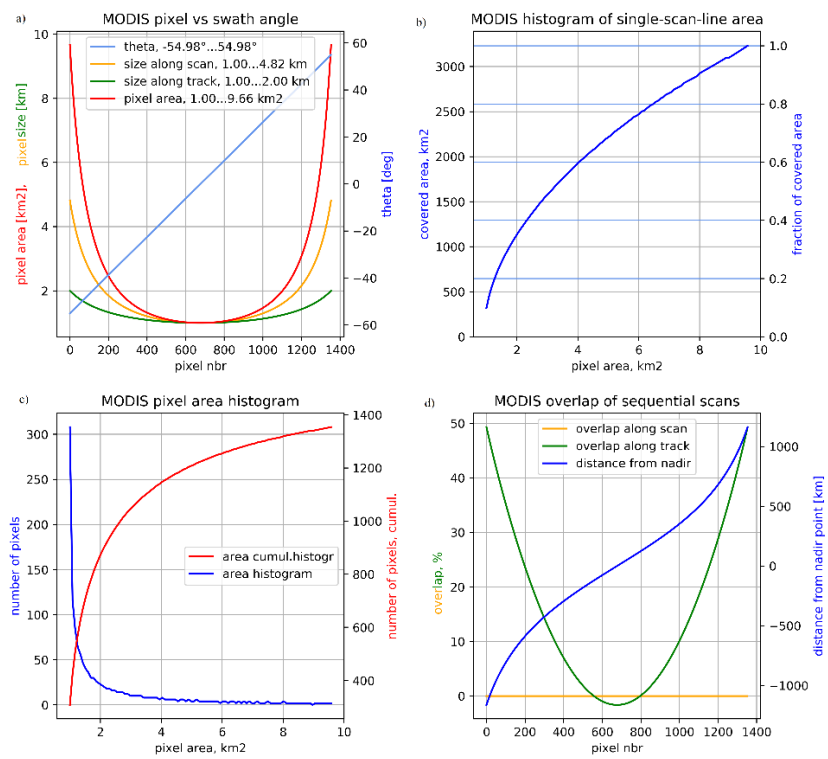

Figure 1. MODIS swath geometry. Panels: a) linear sizes, area, and viewing angle along the scan; b): fraction of swath covered by pixels smaller than the given area; c): distribution of pixel area; d): overlap of pixels along the track and along the scan.

The VIIRS swath geometry (Figure 2) is generally similar but with peculiarities. To limit the pixel size growth along the scan direction, individual pixels of both I- and M-bands are aggregated as 3 × 1 (three scan-direction samples by one track-direction sample), 2 × 1, and 1 × 1 for the scan angles of 0°–30°, 30°–45° and 45°–55°, respectively (Figure 1 in Schroeder et al. (2014b)).

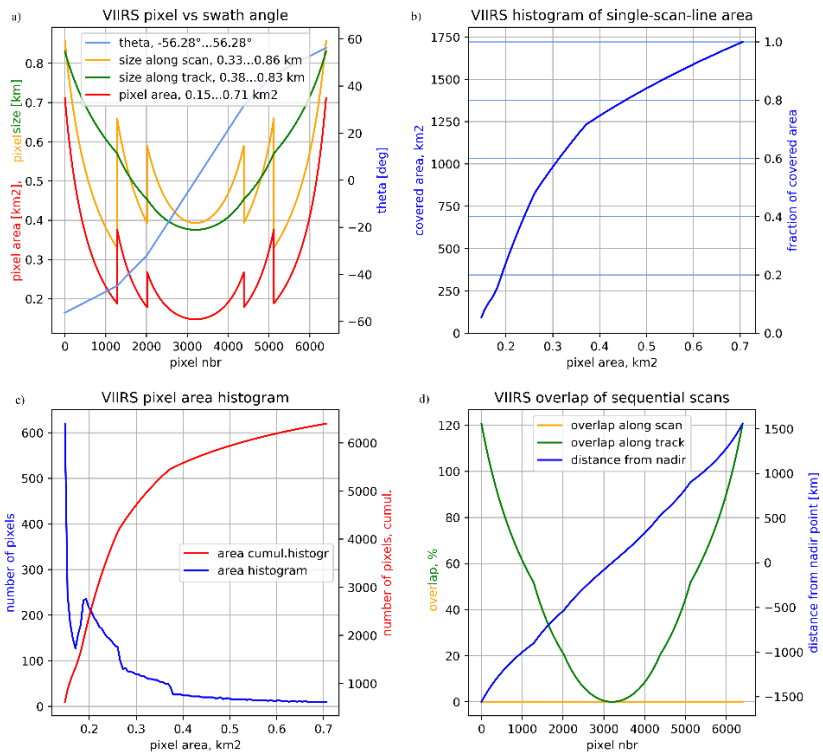

Figure 2. VIIRS swath geometry. Panels: a) linear sizes, area, and viewing angle along the scan; b): fraction of swath covered by pixels smaller than the given area; c): distribution of pixel area; d): overlap of pixels along the track and along the scan.

A single VIIRS sensor has 32 I-band sensors in the track direction, and subsequent scans substantially overlap at high scan angles leading to up to a triple coverage at the edge of the swath. To reduce the redundancy and to limit the amount of data to transfer, data readings from two and four I-detectors from the top and bottom of the arrays (the largest scan angles) are not transmitted in the 2 × 1 and 1 × 1 aggregation zones, respectively (a “bow-tie deletion”). The current study used data of the higher-

resolution I-band detectors, which provide ~375 m nadir pixel size (Wolfe et al., 2013), and explicitly accounted for the pixel aggregation and the bow-tie deletion (Figure 1).

3.3. Pixel-wise and gridded statistics of retrievals

Since all considered satellites are on sun-synchronous orbits and because the fires are heavily influenced by the local diurnal cycle, the analysis was performed in local solar time (LST). Two types of statistics were computed: for individual pixels and for gridded data.

3.3.1. Pixel-wise detection limit

The pixel-wise assessment was performed independently for MODIS and VIIRS. Since it was made with regard to the pixel area (not viewing angle), there was no difference between the procedures, only numerical constants were instrument specific. For individual pixels, the following classification flags were adopted throughout the computations: missing data, cloud, sun glint, non-fire, fire. Areas outside the swath were considered missing.

The pixel detection limit was computed as follows (Figure 3, Figure 4). The retrievals of each instrument were aggregated to four 2-D distribution density functions: for daytime, nighttime, and whole-day FRP $\pi_f(A_p, P_f)$, and for the whole-day number of fire pixels $\pi_n(A_p, P_f)$. Here, A_p is pixel area, P_f is fire radiative power registered by an individual pixel at a single overpass. The obtained distributions are shown in Figure 3 and Figure 4 for MODIS and VIIRS, respectively.

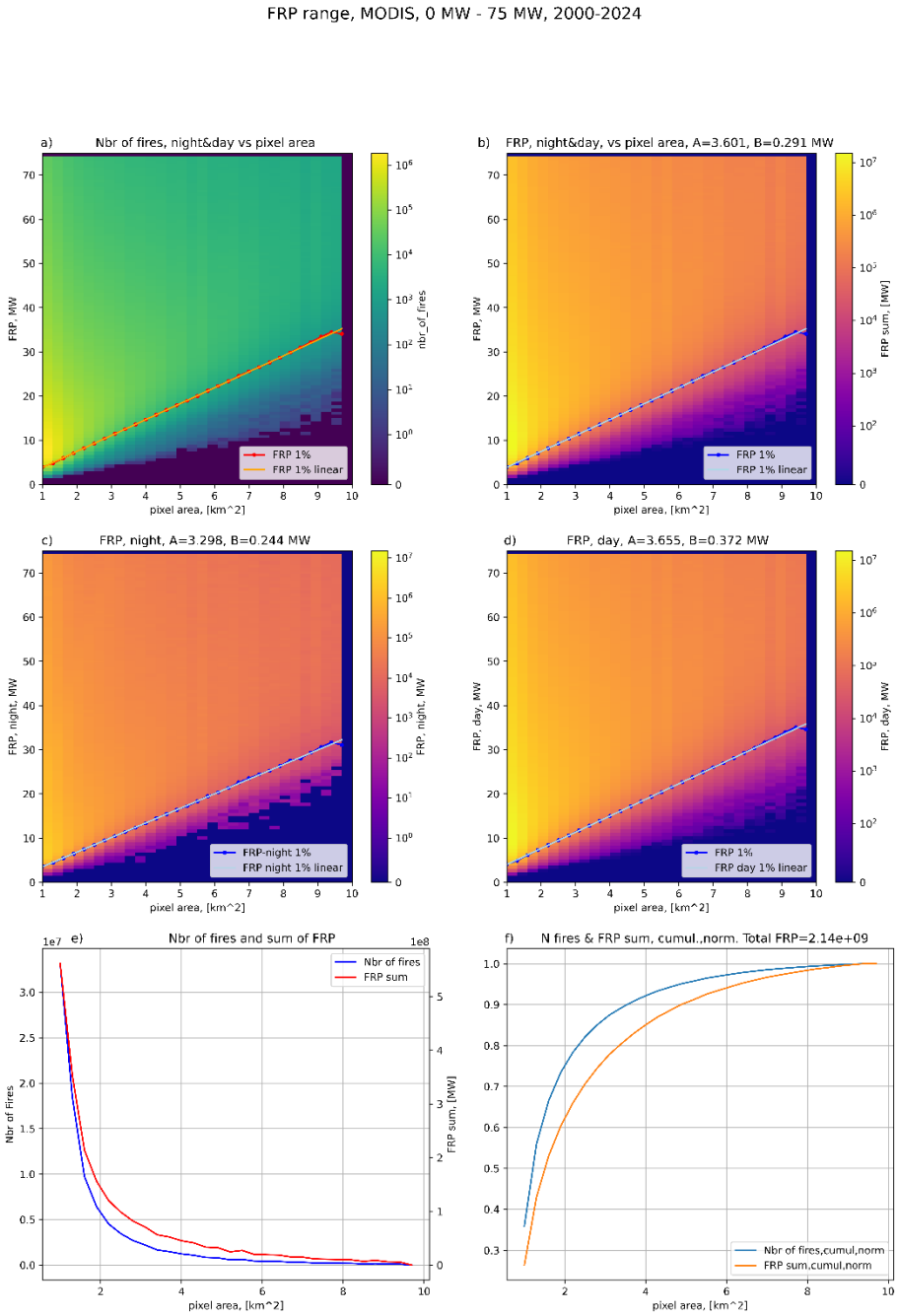

Figure 3. Distribution of the fire pixels detected by MODIS below 75 MW (arbitrarily taken cut-off allowing to see the peaks of the distributions and detection limits) as a function of a pixel size and FRP. Panel a) Total number of fire pixels for all overpasses, b) Total FRP of all overpasses, c) Total FRP registered by night-time overpasses; d) Total FRP registered by day-time overpasses; e) Total FRP and number of fire pixels of the specific area, all FRP values counted (no upper limit); f) same as e) but cumulative. Panels a)-d): red dots represent the 1%-tile for each pixel area whereas the orange lines on top of them represent the corresponding linear approximations, which slope A and intercept B are shown in the panel titles.

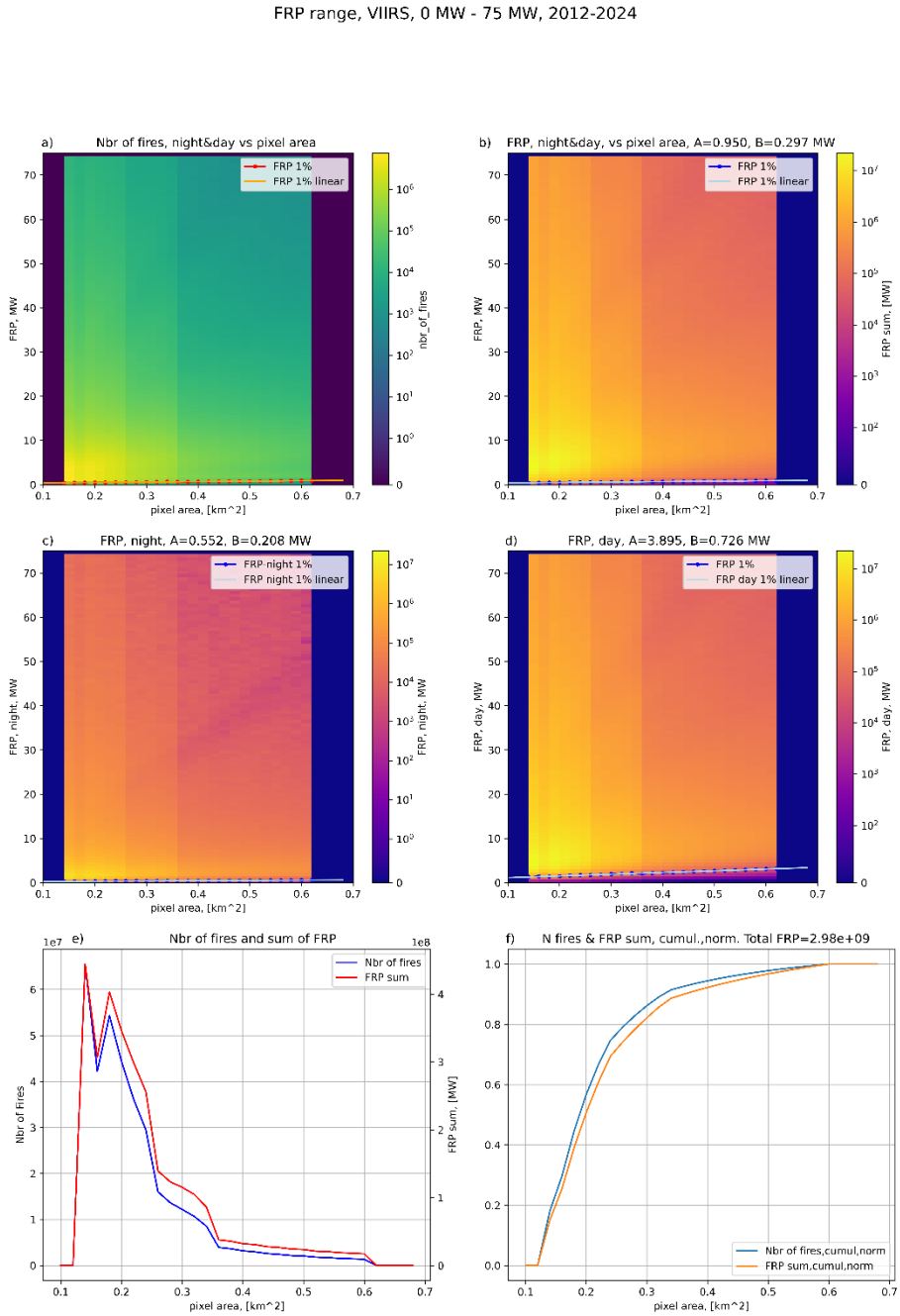

Figure 4. Distribution of the fire pixels detected by VIIRS as a function of the pixel area and FRP. Same panels as for *Figure 3*. Panel a) Total number of fires for all overpasses, b) Total FRP of all overpasses, c) Total FRP registered by night-time overpasses; d) Total FRP registered by day-time overpasses; e) Total FRP and the number of fires registered by the pixels of the specific size, all FRP values counted (no upper limit); f) same as e) but cumulative. Panels a)-d): red dots represent the 1%-tile for each pixel area whereas the orange lines on top of them represent the corresponding linear approximations, which slope A and intercept B are shown at the panel titles.

Detection limit identification was based on the vertical cross-sections of the FRP distribution densities $\pi_f(A_p, P_f)$ (panels c and d in Figure 3 and Figure 4) for each specific pixel size (Figure 5 for MODIS and Figure 6 for VIIRS). The noise in the curves for large FRP is due to the low number of fires falling into the corresponding FRP ranges. The left sides of the curves in panels a) and b) of Figure 5 and Figure 6 can be approximated by a rising logistic function, shifted downward and cut at zero to remove the very small FRP values from the fit and then rescaled to reach max of 1.0:

$$P_{tot}(P_f) = P_0 + \frac{1}{a - c_o} max\left(0, \frac{a}{1 + e^{-r_p(P_f - D_p)}} - c_o\right) \quad (4)$$

Here, P_{tot} is total FRP registered for the corresponding range of P_f, P_0 and a are coefficients of the fit, D_p is the mid-point of the rising sigmoid curve, [MW], and r_p is rate of the function rise, [MW^{-1}], c_o is cut-off. Their values are given under each panel of Figure 5 and Figure 6. As one can see, the shifted logistic-function approximations turned very accurate for all curves (if the noise is smoothed, $r^2 > 0.95$ in all cases and normalized RMSE < ~0.1%).

From the Eq. (4), the definition of the detection limit naturally comes as the position of the midpoint D_p of the rising logistic function. For fires of such power, the total FRP registered by the instrument with the pixels of the corresponding size is half of the histogram max value for that size. It corresponds to ~50% of fires of this intensity missed by the instrument. Dependence of D_p and r on the pixel area A (panel c), $D_p(A_p)$, is a linear function of the pixel area (correlation coefficient > 0.999):

$$D_p = \begin{cases} \infty & for\ pixel\ flagged\ as\ missing \\ \lambda_{lst} A_p + \mu_{lst} & for\ \ pixel\ \ with\ a\ valid\ \ retrieval \end{cases} \quad (5)$$

The coefficients λ_{lst}, μ_{lst} of the Eq. (5) are shown in Figure 5c and Figure 6c and summarized in Table 1 for MODIS and Table 2 for VIIRS. The dependencies of the sigmoid max slope on pixel size are well approximated by hyperbolas.

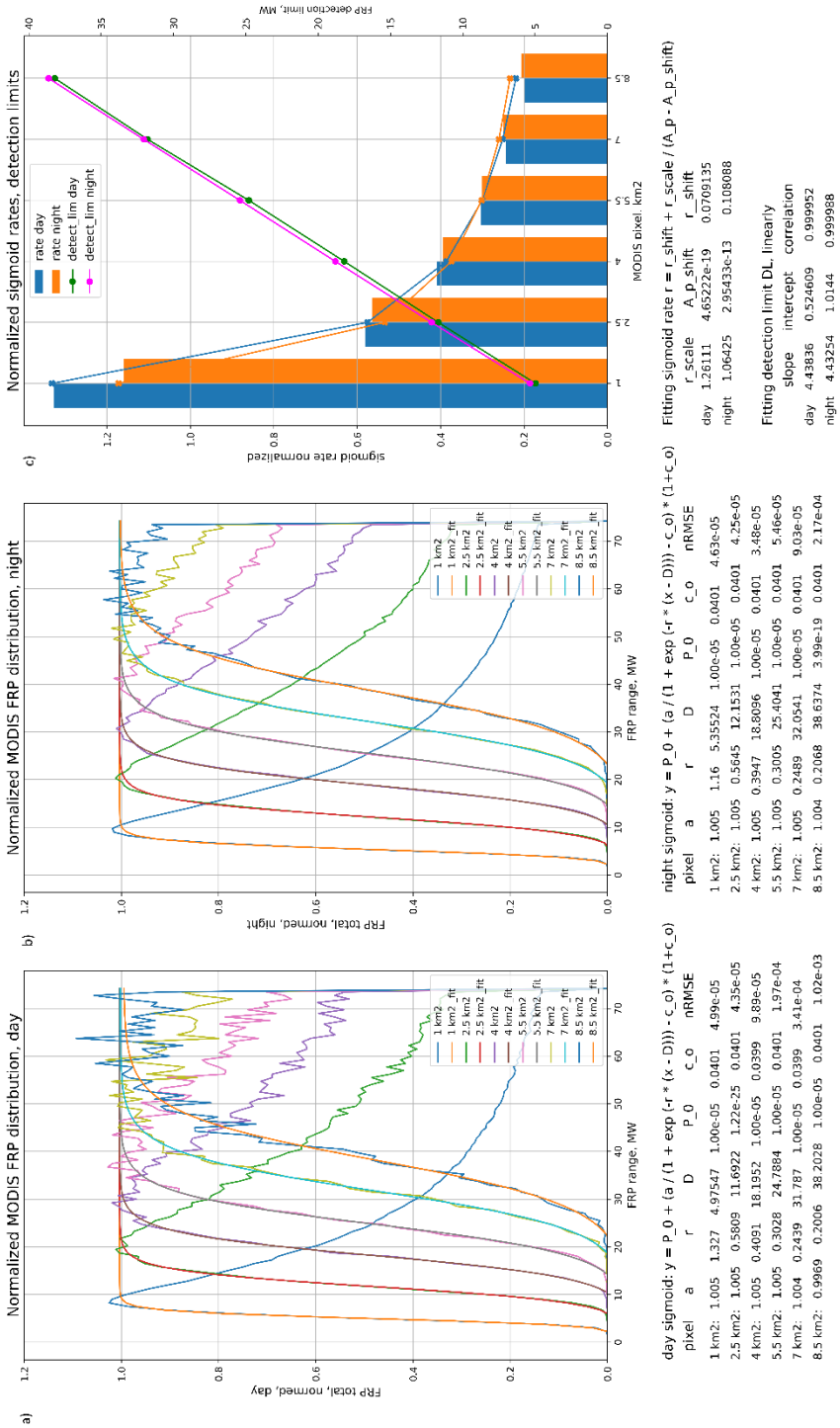

day sigmoid: y = P_0 + (a / (1 + exp (-r * (x - D))) - c_o) * (1+c_o)

pixel	a	r	D	P_0	c_o	nRMSE
1 km2:	1.005	1.327	4.97547	1.00e-05	0.0401	4.99e-05
2.5 km2:	1.005	0.5809	11.6922	1.22e-25	0.0401	4.35e-05
4 km2:	1.005	0.4091	18.1952	1.00e-05	0.0399	9.89e-05
5.5 km2:	1.005	0.3028	24.7884	1.00e-05	0.0401	1.97e-04
7 km2:	1.004	0.2439	31.787	1.00e-05	0.0399	3.41e-04
8.5 km2:	0.9969	0.2006	38.2028	1.00e-05	0.0401	1.02e-03

night sigmoid: y = P_0 + (a / (1 + exp (-r * (x - D))) - c_o) * (1+c_o)

pixel	a	r	D	P_0	c_o	nRMSE
1 km2:	1.005	1.16	5.35524	1.00e-05	0.0401	4.63e-05
2.5 km2:	1.005	0.5645	12.1531	1.00e-05	0.0401	4.25e-05
4 km2:	1.005	0.3947	18.8096	1.00e-05	0.0401	3.48e-05
5.5 km2:	1.005	0.3005	25.4041	1.00e-05	0.0401	5.46e-05
7 km2:	1.005	0.2489	32.0541	1.00e-05	0.0401	9.03e-05
8.5 km2:	1.004	0.2068	38.6374	3.99e-19	0.0401	2.17e-04

Fitting sigmoid rate r = r_shift + r_scale / (A_p - A_p_shift)

	r_scale	A_p_shift	r_shift
day	1.26111	4.65222e-19	0.0709135
night	1.06425	2.95433e-13	0.108088

Fitting detection limit DL, linearly

	slope	intercept	correlation
day	4.43836	0.524609	0.999952
night	4.43254	1.0144	0.999988

Figure 5. Definition of the detection limit as a function of pixel area via the normalized FRP distribution. Colored broken lines at panels a) and b) are the normalized vertical cross-sections of the panels c) and d) of the *Figure 3*, for day and night retrievals, respectively. All curves have been normalized to their smoothed max values. The rising part of each curve is approximated by a sigmoidal function with parameters shown under the panel. Panel c): broken lines show FRP values corresponding to 0.5-level of the corresponding sigmoidal function of the panels a) and b) – the detection limit for the specific pixel size; bars: slope of the sigmoid at those points.

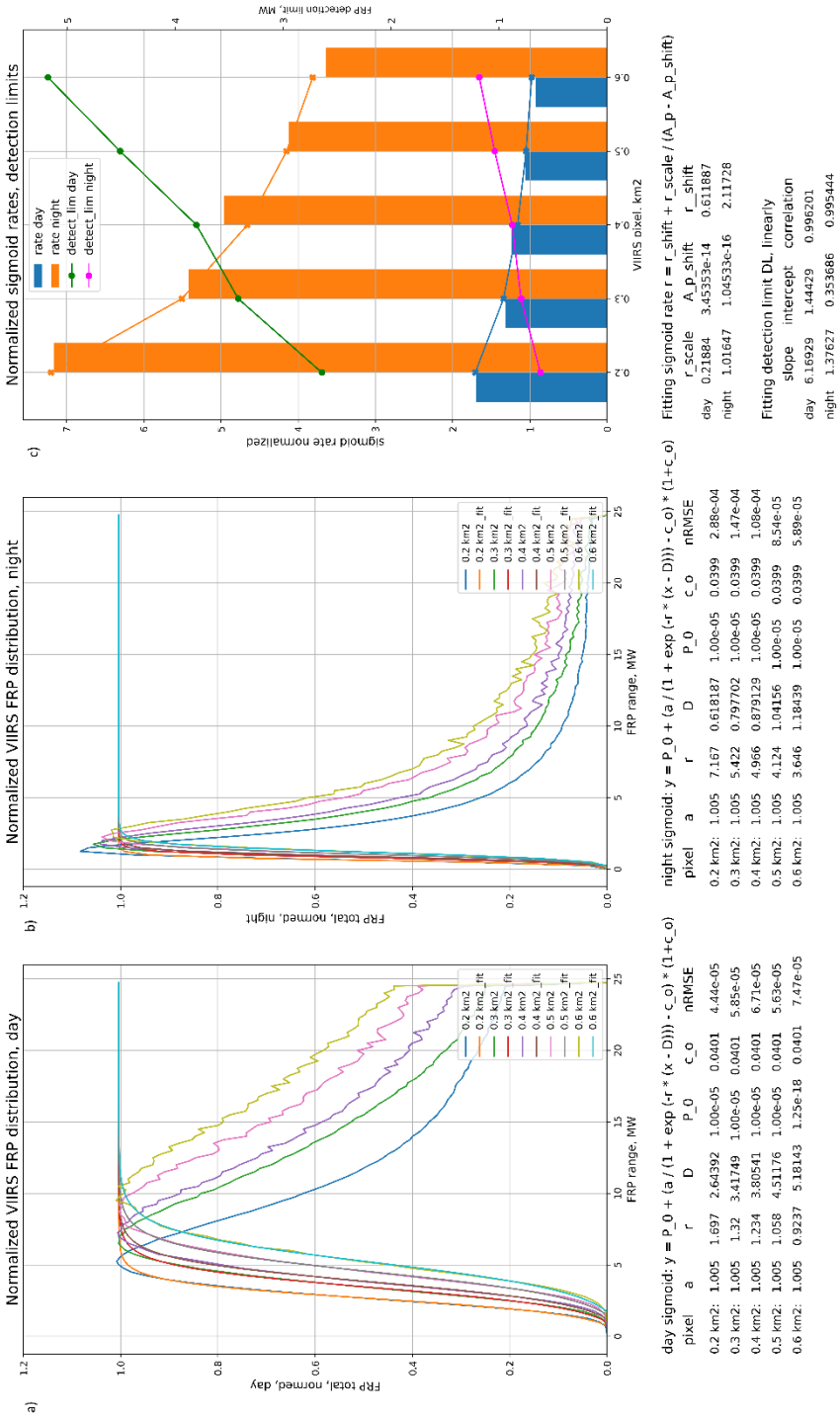

day sigmoid: y = P_0 + (a / (1 + exp (-r * (x - D))) - c_o) * (1+c_o)

pixel	a	r	D	P_0	c_o	nRMSE
0.2 km2:	1.005	1.697	2.64392	1.00e-05	0.0401	4.44e-05
0.3 km2:	1.005	1.32	3.41749	1.00e-05	0.0401	5.85e-05
0.4 km2:	1.005	1.234	3.80541	1.00e-05	0.0401	6.71e-05
0.5 km2:	1.005	1.058	4.51176	1.00e-05	0.0401	5.63e-05
0.6 km2:	1.005	0.9237	5.18143	1.25e-18	0.0401	7.47e-05

night sigmoid: y = P_0 + (a / (1 + exp (-r * (x - D))) - c_o) * (1+c_o)

pixel	a	r	D	P_0	c_o	nRMSE
0.2 km2:	1.005	7.167	0.618187	1.00e-05	0.0399	2.88e-04
0.3 km2:	1.005	5.422	0.797702	1.00e-05	0.0399	1.47e-04
0.4 km2:	1.005	4.966	0.879129	1.00e-05	0.0399	1.08e-04
0.5 km2:	1.005	4.124	1.04156	1.00e-05	0.0399	8.54e-05
0.6 km2:	1.005	3.646	1.18439	1.00e-05	0.0399	5.89e-05

Fitting sigmoid rate r = r_shift + r_scale / (A_p - A_p_shift)

	r_scale	A_p_shift	r_shift
day	0.21884	3.45353e-14	0.611887
night	1.01647	1.04533e-16	2.11728

Fitting detection limit DL, linearly

	slope	intercept	correlation
day	6.16929	1.44429	0.996201
night	1.37627	0.353686	0.995444

Figure 6. Definition of the FRP detection limit as a function of pixel size via the normalized FRP distribution for VIIRS. Panels are the same as in *Figure 5*. Colored broken lines at panels a), b) are the normalized vertical cross-sections of the panels c) and d) of the *Figure 4* for day and night retrievals, respectively. All curves have been normalized to their smoothed max values. The rising part of each curve is approximated by a sigmoid function with parameters shown under the panel. Panel c) broken lines: FRP values corresponding to 0.5 levels of the corresponding sigmoid function of panels a) and b) – the detection limit for the specific pixel size; bars: slope of the sigmoid at those points

Table 1. Coefficients for the pixel-wise MODIS Observation Operator, Eqs. *(5)* - *(7)*

	Day: $\phi < 90°$	Night: $\phi \geq 90°$
λ_{lst} (slope), [MW km^{-2}]	4.44	4.43
μ_{lst} (intercept), [MW]	0.52	1.01
r_0 (shift), [MW^{-1}]	0.07	0.11
r_1 (scale), [km^2 MW^{-1}]	1.26	1.06
c_0 (cut-off)	0.045	0.045

Table 2. Coefficients for the VIIRS pixel-wise Observation Operator, Eqs. *(5)* - *(7)*

	Day: $\phi < 90°$	Night: $\phi \geq 90°$
λ_{lst} (slope), [MW km^{-2}]	6.17	1.38
μ_{lst} (intercept), [MW]	1.44	0.35
r_0 (shift), [MW^{-1}]	0.61	2.12
r_1 (scale), [km^2 MW^{-1}]	0.21	1.02
c_0 (cut-off)	0.05	0.05

Figure 5c and Figure 6c show that the slope of the rising sigmoid of the Eq. (4) is a hyperbolic function of the pixel size:

(6)
$$r_p = r_0 + \frac{r_1}{A_p - A_0}$$

For other coefficients, as follows from the fitting coefficients in Figure 5a,b and Figure 6a,b, the very small value of P_0 can be neglected, and the coefficient a set to 1.0.

Finally, replacing P_f with a model-predicted P_{mdl}, we obtain the observed FRP P_{obs} as a function of predicted P_{mdl}, thus concluding the pixel-wise observation operator $\Xi_{pix}(P_{mdl})$:

(7)
$$P_{obs}(P_{mdl}) \triangleq \Xi_{pix}(P_{mdl}) = \frac{P_{mdl} * 1}{1 - c_o} max\left(0, \frac{1}{1 + e^{-r_p(P_{mdl} - D_p)}} - c_o\right)$$

3.3.2. Grid-cell-wise detection limit

This section introduces the OOp for models operating on a regular grid and with a regular time step. The grid cell size d is assumed to be significantly larger than the MODIS or VIIRS pixels. The grid-cell FRP $P(i,j)$ is a sum of FRPs of pixels in this cell: $P(i,j) = \sum_{(i,j)} P_f$. Evidently, the grid-cell fire detection is determined by the highest P_f – that very pixel has the highest chances to be noticed by the satellite. A mean fraction of the strongest fire pixel in the grid cell, $\gamma(d,P) = \overline{P_f/P}$, can be found from MODIS and VIIRS statistics as a function of $d \wedge P$ (Figure 7).

As seen from Figure 7, for grids coarser than 0.5°, γ depends only on total FRP $P(i,j)$: the curves corresponding to different d coincide. For fine grids, γ is larger reaching unity when grid cell size becomes similar to that of individual pixels. We approximated this 2-D dependency as follows:

$$\gamma = 1 - \left[1 - \left(\frac{P_2 - P_1}{P(i,j) - P_1} exp\left(\frac{d_1}{d}\right)\right)^{k_1}\right]^{k_2} \quad (8)$$

Here, d is grid resolution, d_1 is its empirical scaling, P_1, P_2, are FRP scaling constants, [MW], k_1, k_2 are dimensionless empirical constants. Both MODIS and VIIRS FRP retrievals can be approximated with this formula (Figure 7). The only difference is that VIIRS detects almost four times more small fires than MODIS, thus reducing the contribution of the strongest fire pixel by approximately 50%.

For a clear-sky grid cell, it is natural to use an area-weighted spatial average of detection limits over the pixels in the cell and account for the fraction of the largest fire in the total FRP:

$$D_{clr_{sky}}(i,j) = \frac{\sum_{p\in(i,j)} D_p A_p}{\gamma \sum_{p\in(i,j)} A_p} \quad (9)$$

a)

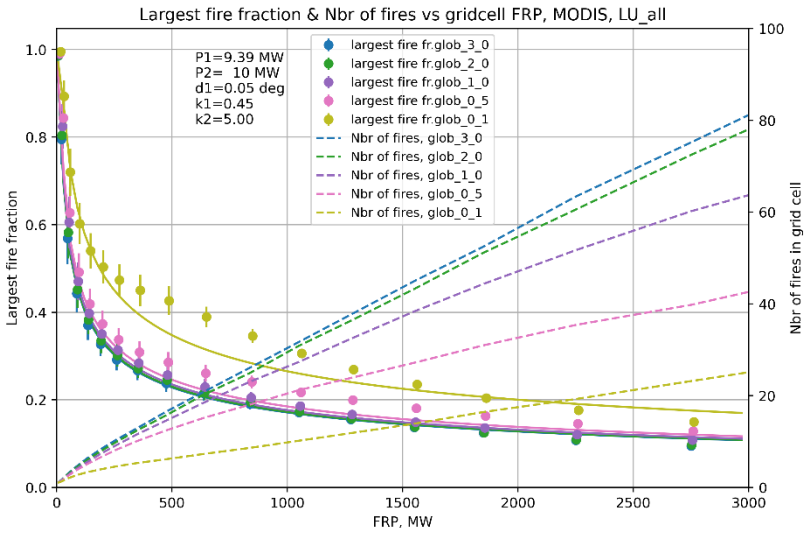

b)

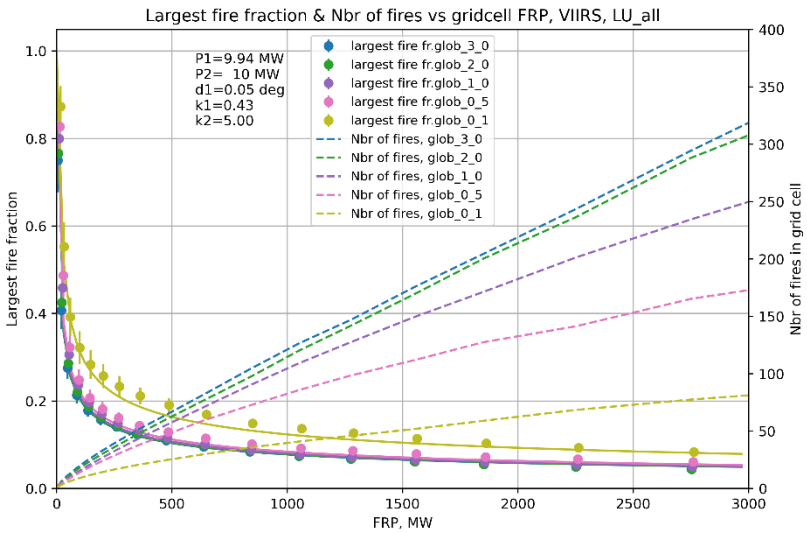

Figure 7. A mean fraction γ of the largest fire pixel in the total grid-cell FRP *P,* as a function of *P*. Calculated from MODIS 2000-2023 time series (panel a) and VIIRS 2018-2024 (panel b) as a function of grid-cell FRP for different grid resolutions *dx*. Fitting curves are computed from the Eq.*(8)* with the coefficients shown at the plot. Charts and dots are slightly shifted horizontally to reduce overlapping.

For accounting for the partial obscuration of the grid cells, the following rules have been applied:

- for a grid cell *(i,j)*, the gridded fire radiative power is $P(i,j) = \sum P_f$ – a sum of all pixels within the grid cell *(i,j);*
- a fraction of the grid cell retrieved area, β_{ret}, is calculated from the pixel state flags as a fraction of the cell covered with pixels flagged as fire or non-fire, (i.e. not missing, cloudy, or sun-glint)

The grid-cell detection limit D_g is computed as a sum of the clear-sky detection limit D_{clr_sky} (9) and a term inversely proportional to β_{ret}, thus approaching infinity for a fully cloudy grid cell. Formally, it can be written as follows:

$$D_g(i,j) = \frac{\sum_{p\in(i,j)} D_p A_p}{\gamma \sum_{p\in(i,j)} A_p} + P_{max}\left(1 + exp\left(\frac{\beta_{ret}(i,j)}{\sigma_{ret}}\right)\right)^{-1} \quad (10)$$

The summation in the first term is taken over all non-missing MODIS pixels *p* of the grid cell *(i,j)*, P_{max} is a large FRP value, e.g., 10 GW, and σ_{ret} is a width of the transition range of the logistic function, e.g., 0.1. With such parameters, the second term is practically zero for $\beta_{ret} > 0.3$ but quickly grows approaching 5 GW if the grid cell has fewer valid pixels. The very high but still finite detection limit for cloudy scenes is taken to avoid numerical problems at the implementation stage.

With D_g from (10), the observed grid-cell FRP $P_{obs}(i,j)$ can be computed similarly to the pixel-wise OOp:

$$P_{obs}\big(P_{mdl}(i,j)\big) \triangleq \Xi_{grd}\big(P_{mdl}(i,j)\big) = \frac{P_{mdl}(i,j)}{1 + e^{-r_g\left(P_{mdl}(i,j) - D_g(i,j)\right)}} \quad (11)$$

The sigmoid slope r_g can be calculated as an area-weighted mean value for the pixels in the grid cell or simply taken as a prescribed instrument-specific constant representing a “typical” swath geometry (Table 3). Additional uncertainties due to this simplification are much smaller than those of the cloud-related term in the Eq. (10).

Table 3. Suggested "typical" slope r_g for Eq. (11)

	Day: $\phi < 90°$	Night: $\phi \geq 90°$
r_g MODIS, [MW km^{-2}]	0.5	1.2
r_g VIIRS, [MW km^{-2}]	1.5	15

3.4. Thin clouds and smoke obscuration

In the above derivations, it is assumed that fire is either obscured by a cloud or not. However, the cloud can be thin, or a fire can be dimmed by its own smoke or other aerosols. The satellite would then process the pixel like a non-obscured one, but the signal strength would be lower. Denoting aerosol column optical depth (AOD) at the wavelength of the fire detection (4 μm for MODIS and VIIRS, Eq. (6) in (Giglio et al., 2016)) as τ_4, one should replace the model-predicted FRP P_{mdl} with $P_{\widetilde{mdl}}$ in (7) and (11):

$$P_{\widetilde{mdl}} = P_{mdl} \exp(-\tau_4) \quad (12)$$

All other terms remain the same. This approach should be considered as indicative because aerosol obscuration will impact the retrieval at other wavelengths too thus influencing the fire detection / rejection procedure and indirectly affecting the gridded FRP (see Table 1, (Giglio et al., 2016) and Section 3 of (Schroeder et al., 2014b)).

3.5. Application of the OOp for comparison of the satellite datasets

The OOp has been developed for projecting a model-predicted FRP onto the observational space, but it can also be used for projecting one FRP dataset onto another. A complexity, however, is that the OOp implies a space-time co-location of the datasets, which is impossible for the low-orbit satellites. For instance, the accurate spatial co-location of MODIS AQUA and VIIRS Suomi NPP retrievals is straightforward, but their retrieval times differ by 1–2 hours, leading to different cloud obscuration and fire stages. The imperfect temporal co-location can be accounted for by symmetric OOp application:

- For a given day, select overlapping granules of MYD14 & MYD35 of MODIS Aqua and VNP14 & VNP03 of VIIRS Suomi NPP
- Scan the overlapping areas picking MODIS active-fire pixels and VIIRS active-fire pixels
- Project each MODIS fire pixel to the corresponding VIIRS granule, collect VIIRS fire observations and missing cell fractions corresponding to this MODIS fire pixel
- Project each VIIRS fire pixel to the corresponding MODIS granule, collect MODIS fire observations and missing cell fractions corresponding to this VIIRS pixel
- Apply MODIS pixel-wise OOp, Eq. (7) Table 1, to each active fire of VIIRS accounting for the MODIS missing pixels, thus obtaining $\Xi_{pixMODIS}(P_{VIIRS})$
- Apply VIIRS pixel-wise OOp, Eq. (7), Table 2, to each active fire of MODIS accounting for the VIIRS missing pixels, thus obtaining $\Xi_{pixVIIRS}(P_{MODIS})$
- compare the obtained datasets:

$$\Xi_{pixMODIS}(P_{VIIRS}) \quad \text{vs} \quad \Xi_{pixVIIRS}(P_{MODIS}) \tag{13}$$

Here, $\Xi_{pix}(P)$ is the pixel-wise OOp, Eq. (7).

4. Examples of the OOp applications

4.1. Application of grid OOp to retrieve cloud obscuration statistics

The cloud-related term in Eq. (10) leads to a space-dependent probability of missing a fire regardless of its intensity. A rough estimate of such probability is a mean of $(1 - \beta_{ret})$ for a particular region (see Eq. (10) for definition of β_{ret}), averaged over the satellite overpasses (Figure 8a, mean fraction of missing pixels in the MODIS granules). This fraction is computed from MxD35 and Vxx03 products for MODIS and VIIRS, respectively. Pixels with “sunglint” or “cloud” flags are considered missing. However, this fraction

should be considered as the upper estimate of $(1 - \beta_{ret})$ because fires tend to occur in dry periods when the cloud cover (the main reason for missing observations) is lower than the annual mean.

A way to account for the mutual anticorrelation of clouds and fire occurrences is to calculate the mean cloud cover only during a fire season in the region. A quantitative criterion can be the non-zero sum of FRP for the surrounding area of, for instance, 1°×1° (Figure 8b for MODIS and Figure 8c for VIIRS).

Due to anticorrelation between cloud cover and detection probability, the missing fractions in Figure 8b,c, being more realistic than the mean cloud cover of Figure 8a, probably underestimate the omission error, thus being the lower estimate of the omission probability.

The results in Figure 8 depend on the arbitrarily selected size of the inspected area around the cloudy grid cell. Impact of this area has been quantified via a sensitivity study by varying it from 0.1° up to 20° (Figure 9). Calculations showed low sensitivity, e.g., doubling the area from $1° \times 1°$ to $2° \times 2°$ adds less than 10% to the omission probability of Figure 8 b, c (see also Figure 9). Further expansion eventually leads to the same map as that of Figure 8a (for MODIS). A wider inspected area generally leads to less steep curves and smoother patterns (Figure 9). However, a wide search is not justified: already 200 km is too large as a correlation distance for regional fires. A smaller area leads to a patchy non-representative map.

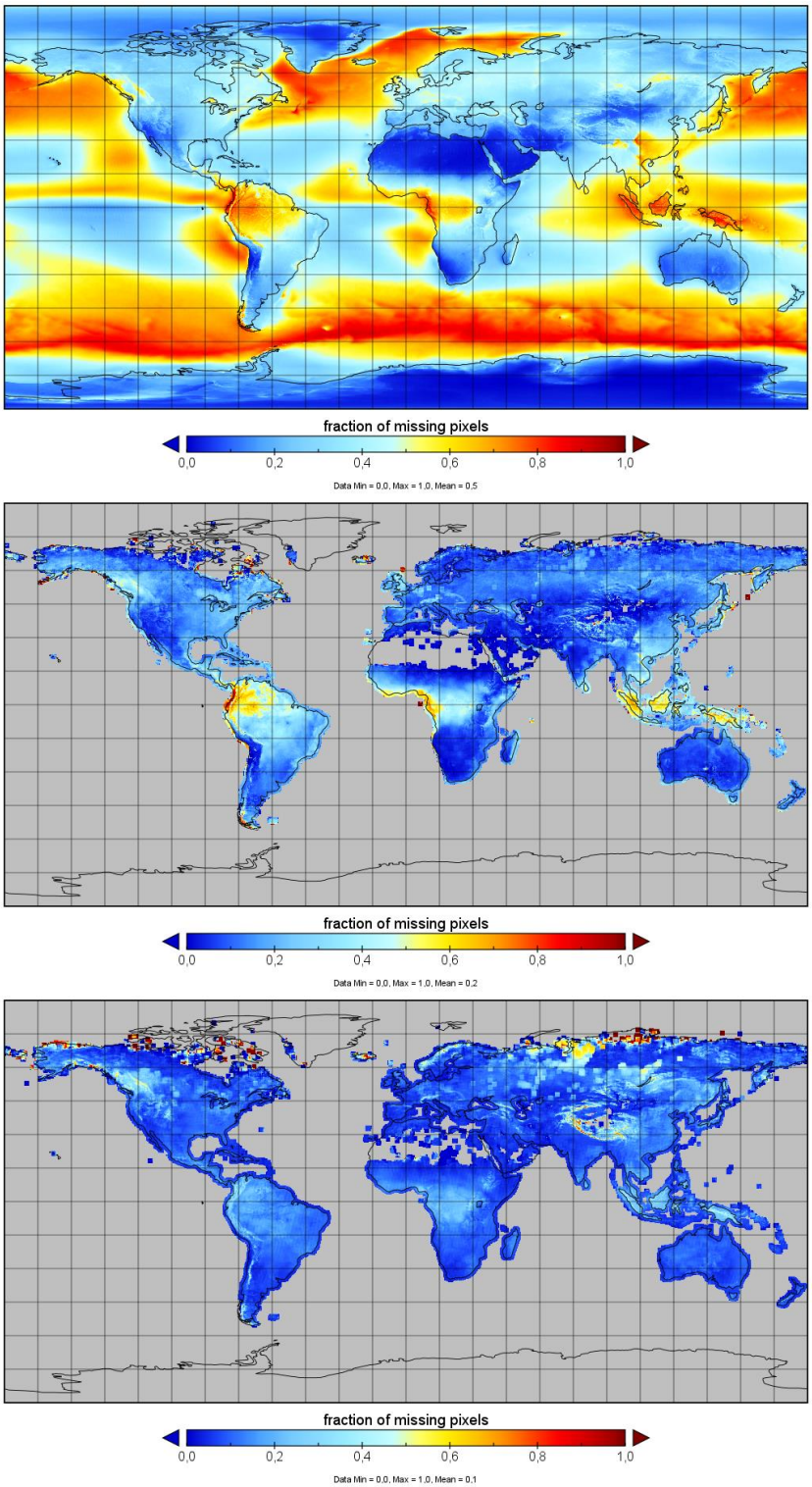

a)

b)

c)

Figure 8. Mean fraction of missing pixels due to cloud obscuration of MODIS, 2000–2020, and VIIRS, 2018–2024. Panel a) mean over all MODIS overpass times, b) mean over hours when non-zero FRP registered by MODIS anywhere in 1° × 1° square centered around the grid cell, c) mean over hours when non-zero FRP registered by VIIRS anywhere in 1° × 1° square centered around the grid cell.

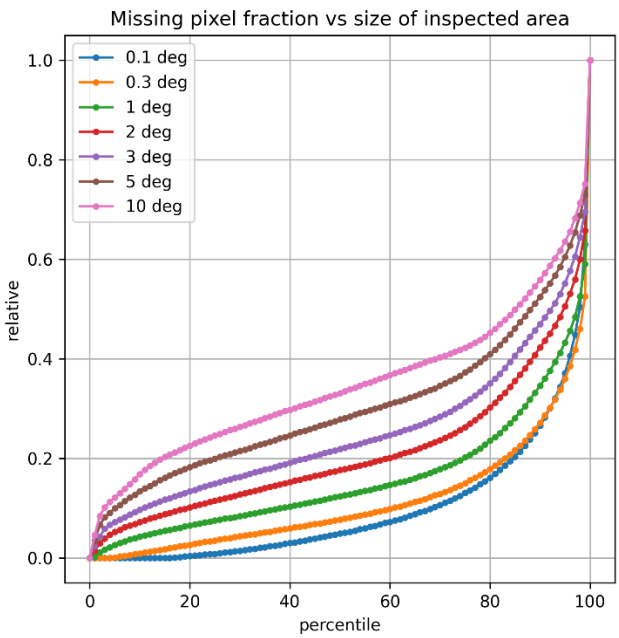

Figure 9. Distribution of mean fraction of MODIS missing pixels for different sizes of area around the detected fire inspected for presence of other fires. The green curve (1 deg area size) corresponds to panel b) of Figure 8. The curve 0.1 deg corresponds to no season checking, whereas the curve "10 deg" is practically equivalent to mean cloud fraction (panel a) in Figure 8). Distribution is calculated only over land and regions with fires (Figure 8, panels b, c)

The maps of Figure 8 suggests that, even during the fire seasons, the omission error of low-orbit satellite instruments like MODIS or VIIRS is typically within 20–40% for most fire-prone regions, with VIIRS showing 10–20% lower omission error than MODIS. In equatorial regions, omissions can be much higher: the fraction of missed fires can exceed 60% for MODIS and 40% for VIIRS.

The lower omission error of VIIRS may be due to (i) higher resolution, (ii) higher sensitivity, as shown in the discussion below, (iii) overpass time in the middle of day when cloudiness may be at its daily lowest level. Another peculiarity of VIIRS is a very high omission in Arctic, where MODIS shows the "usual" 40%. This is caused by the high sensitivity of VIIRS: it detects more fire pixels in partly cloudy conditions and

outside the main fire season. Clouds during these periods then contribute to the VIIRS omission error, whereas MODIS misses them altogether and thus does not consider these times as fire-prone at all.

4.2. Application of OOp to relate VIIRS and MODIS observations

The pixel-wise OOp was applied to the MODIS AQUA and VIIRS Suomi-NPP FRP retrievals for a full year of 2020, taken as an example. The procedure followed the symmetric approach (13). The outcome (example in Figure 10) expectedly showed that VIIRS registered ~30% more FRP than MODIS (panels a), b) Figure 10) due to its lower detection limit. Application of MODIS-based OOp zeroed pixels with small FRP resulting in a 1.5 times lower granule total (panel d). Accounting for the differences in cloudiness via application of VIIRS OOp to the MODIS fire pixels led to ~30% reduction of the total FRP, thus leaving only those locations that were visible for both satellites (panel c).

Analysis of the whole year 2020 brought over 40,000 MODIS AQUA granules with fire pixels registered by at least one instrument. Total FRP retrieved by MODIS and VIIRS within these granules was 128 TW and 177 TW, respectively. Symmetric application of $\Xi_{pixVIIRS}(P_{MODIS})$ and $\Xi_{pixMODIS}(P_{VIIRS})$ lead to 88 TW and 106 TW, respectively. This is illustrated in Figure 11, which compares VIIRS retrievals before and after the MODIS OOp application (P_{VIIRS}, blue dots and $\Xi_{pixMODIS}(P_{VIIRS})$, orange dots) with the MODIS FRP processed by the VIIRS OOp ($\Xi_{pixVIIRS}(P_{MODIS})$, x-axis in Figure 11).

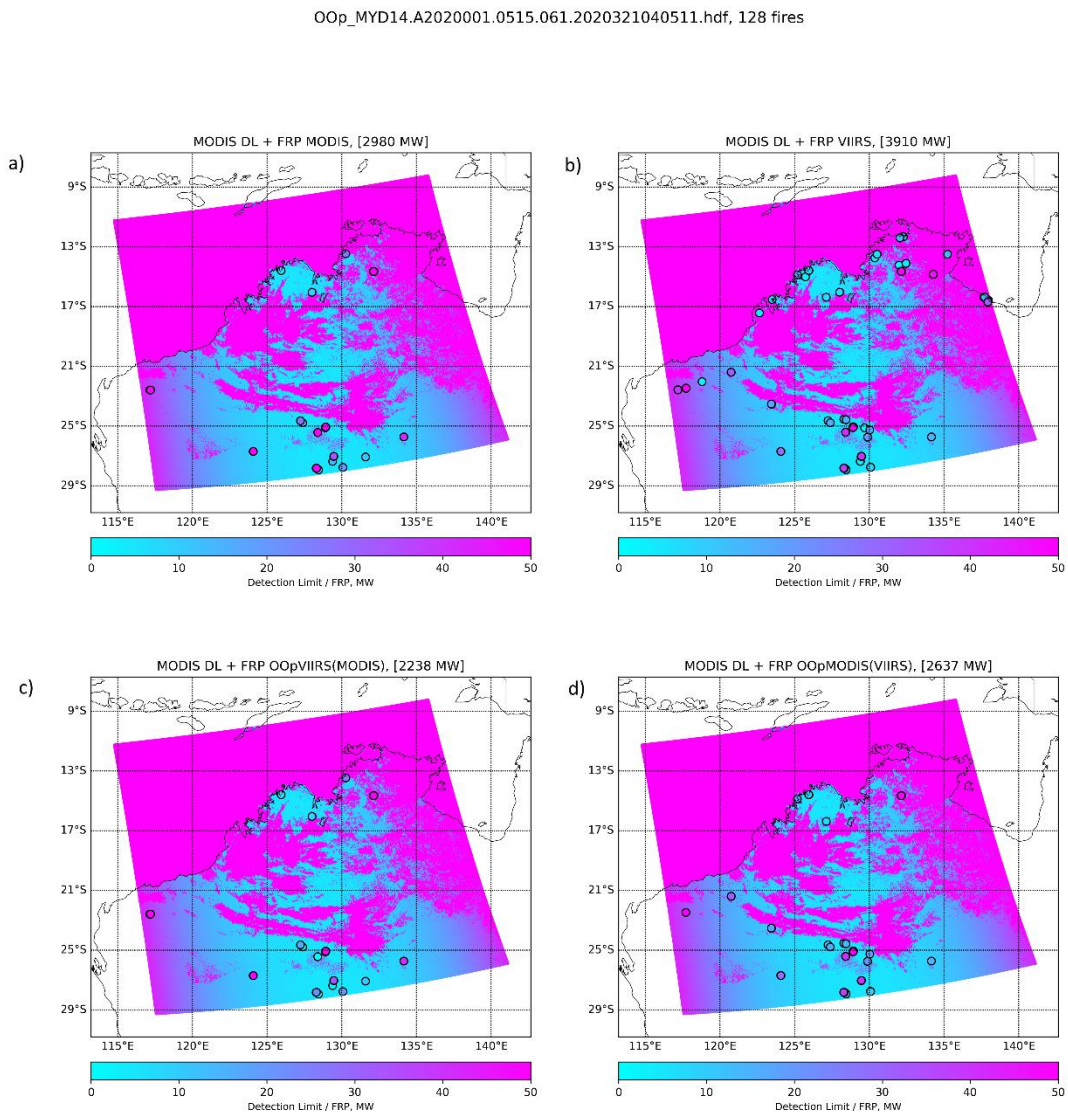

Figure 10. MODIS and VIIRS fire retrievals for a MODIS AQUA granule over North-East Australia, 1.1.2020, 5:15 UTC, [MW]. Background in all panels is MODIS detection limit accounting for larger pixels at the swath edges and cloudiness. Upper panels show MODIS and VIIRS FRP retrievals that fell into that granule, lower panels present the $\Xi_{pixVIIRS}(P_{MODIS})$and $\Xi_{pixMODIS}(P_{VIIRS})$, respectively.

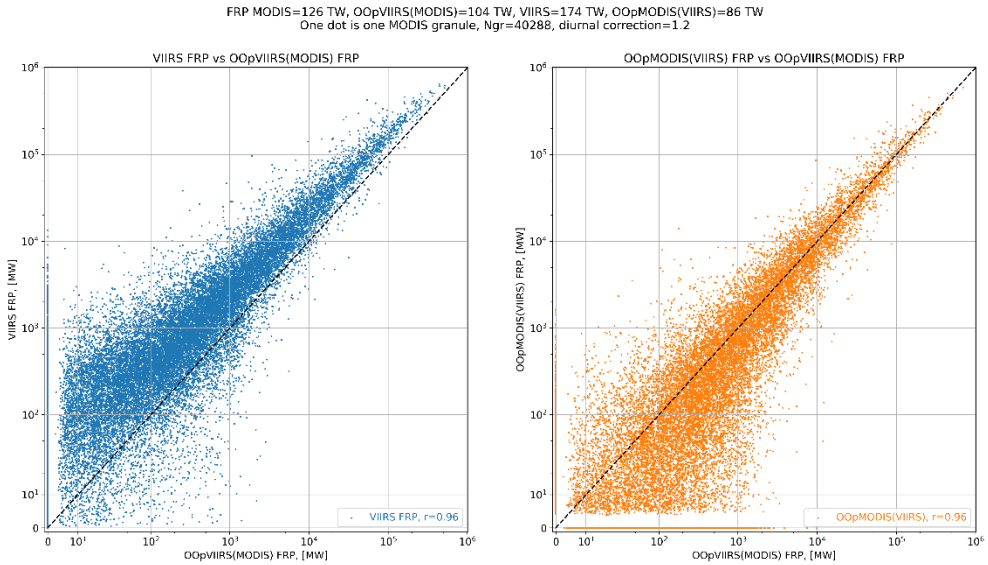

Figure 11. Summary of P_{MODIS} (blue) and $\Xi_{pixMODIS}(P_{VIIRS})$ (orange) for 2020. Each dot represents the total FRP of fires that fell to a single MODIS AQUA granule. Granules that did not have VIIRS coverage (missing or corrupted VIIRS granules) and granules with no fires in both instruments are filtered out. A diurnal variation correction factor 1.2 is applied to VIIRS retrievals (see Discussion section).

The OOp-processed datasets match closely: the initial 38% difference, VIIRS registering more FRP, turns to 20% more OOp-processed FRP of MODIS. This 20% difference originates from different overpass times of the satellites (see the discussion section below), so accounting for it results in a close match of the OOp-processed datasets (Figure 11).

5. Discussion

5.1. Features of the pixel-wise detection limit and OOp of MODIS and VIIRS FRP retrievals

The first percentiles of the distribution densities $\pi_f(A_p, P_f)$ and$\pi_n(A_p, P_f)$ (Figure 3, Figure 4) (the red-dots and orange regression lines) are linear functions of the pixel area for both MODIS and VIIRS, with correlation coefficient >0.99. For both satellites, the 1st percentile of the nighttime FRP is lower than that of daytime, for all pixel sizes, with the difference being larger for VIIRS than for MODIS.

The panels e) and f) of the figures show that the smallest pixels register most of the FRP and the total number of fires. For MODIS, 50% of fires are from 1–1.2 km^2 area pixels while the fraction of the swath covered by such pixels is about 20% (see the swath geometry in Figure 1b, c). For VIIRS, pixels < 0.3 km^2 occupy 60% of the swath area but provide ~90% of fire detections (Figure 2b, c).

5.2. Previous assessments of the MODIS/VIIRS omission error and sensitivity to small fires

The results reported above can be compared with case studies presented in literature. For instance, the cloud obscuration of fires in Brazilian Amazon (Schroeder et al., 2007) led to the omission error of 11% for GOES geostationary fire products. This estimate expectedly differs from the MODIS / VIIRS statistics (Figure 8): e.g., the mean cloud cover of MODIS overpasses over that area is 0.4–0.7. For fire seasons, Figure 8b suggests the omission error from 0.2–0.6 for MODIS and 0.1–0.3 for VIIRS. The difference from the value of (Schroeder et al., 2007) refers to the ability of geostationary satellites to follow the fire over time thus avoiding some clouds. As follows from the comparison, it can about-half the omission error, at a price of 16 times lower resolution (GOES sub-satellite pixel was 4 km × 4 km), with the corresponding loss of small- and mid-sized fires.

The only study reporting the dependence of the fire detection probability on the pixel size was made for MxD14 Collection 5 data by (Maier et al., 2013) for Australia. The study suggested that fires with FRP < 3.6 MW are never detected (practically no fires were recorded up to 5 MW) whereas the frequency distribution of FRP is significantly disturbed already at 15 MW. According to the FREEVAL study (Schultz et al., 2008), the minimum-FRP detection threshold for MODIS Collection 4 was about 7–10 W m^{-2} (7-10 MW for 1 km^2 pixel). This is in agreement with the predicted sensitivity limit of 10–20 W m^{-2} of (Kaufman et al., 1998). Finally, our earlier estimates made for Collection 5 (Soares et al., 2015) pointed out that noticeable distortions of the FRP distribution start at 15 W m^{-2}. Except for (Maier et al., 2013), none of these works referred to the pixel size and the overpass time, and should therefore be attributed to the

smallest nadir pixel of MODIS, 1 km^2. These numbers are about-twice higher than the limit obtained above for Collection 6, which confirms the better detection of small fires in Collection 6 in comparison with the earlier Collections.

The dependence of the detection limit on the pixel size is dictated by the geometry of the instrument and the basic principle of the temperature-contrast based fire detection, leading to qualitatively similar dependencies obtained by (Maier et al., 2013) and in the current work. Among the differences, one can notice an almost-perfect linear relation of the detection limit in the current study in contrast to a "saturation" noticed for large viewing angles by Maier et al, who attributed it to the randomly selected 1% threshold. However, in the current study, there is no saturation for 1% threshold either (Figure 3 and Figure 4). A more probable reason is an insufficient number of fire detections in the large-pixel size range: only 57.2 thousand events were counted in the Maier et al analysis vs ~90 million cases for MODIS in this study. Should this saturation be ignored, the detection limit for the largest pixels at the edge of the swath would exceed 55 MW for Collection 5, compared to 42 MW / 39 MW for day/night overpasses for Collection 6 in this study.

5.3. Comparison with sensitivity and detection probability of SEVIRI

The sensitivity of SEVIRI has been evaluated within the FREEVAL project (Schultz et al., 2008). That study concluded that "SEVIRI should be able to confidently detect actively burning fires whose FRP reaches a minimum of around 100 MW, and in certain cases may be able to detect fires whose FRP is even lower than this, down to around 50 MW." That generic conclusion was refined by the fire histogram of the sub-satellite pixels (Figure 4.2 in the FREEVAL report), whose size (3 km $\times$ 3 km) closely matches pixels at the edge of the MODIS swath. In the FREEVAL histogram, strong disturbances start from FRP of 43 MW, with detection limit being between 35–40 MW. This result corroborates very well with the current assessment because the 9 km^2 area corresponds to 40.5–40.9 MW detection limit (day-night) according

to Eq. (5) and Table 1. Therefore, the lowest detection limit of SEVIRI (sub-satellite fires) is 10% lower than the corresponding detection limit of MODIS near the edge of its swath. The difference can originate from the differences in the instruments, the FRP retrieval algorithms, and the accumulated statistics (the FREEVAL SEVIRI histogram is based on 3 months in 2004).

Comparison with VIIRS is not unequivocal. Schroeder et al. (2014b) related the fire size and temperature to the probability of VIIRS to detect it and concluded that a small (1.5 m radius) but hot (1000 K) fire can be noticed at night. In a qualitative agreement with that prediction, a histogram of VIIRS FRP data (Figure 4) suggests ~0.7 MW detection limit at night in the center of the swath.

5.4. Comparison of MODIS and VIIRS

A direct comparison of the detection limit formulas and coefficients for MODIS and VIIRS (Table 1, Table 2, Figure 12) reveals both the effect of the pixel size on the detection limit and the difference between the instruments and processing algorithms: VIIRS is about 3x more sensitive than MODIS for comparable pixel size of ~ 1 km^2 at night, but about 25% less sensitive during day (within 5% for the first percentile).

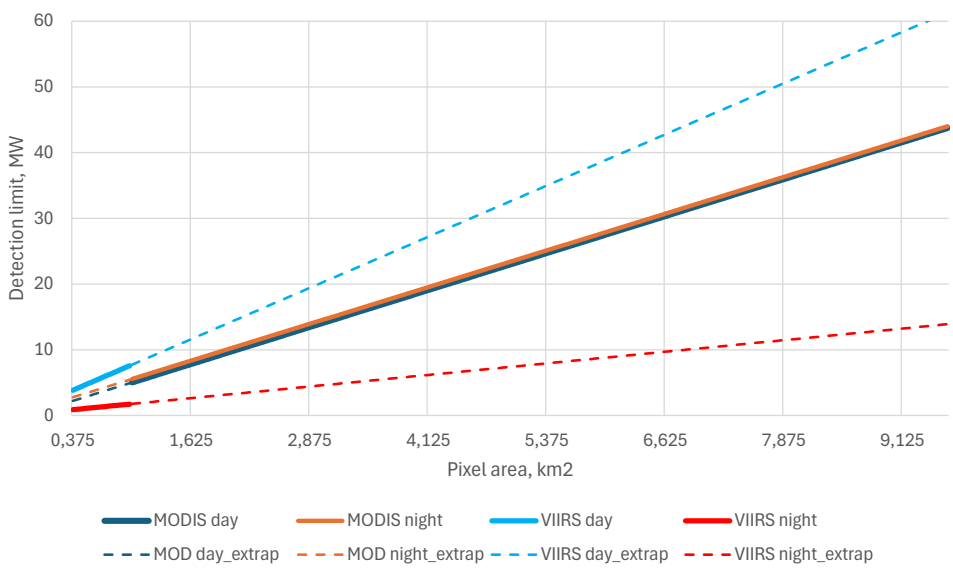

Figure 12. MODIS and VIIRS detection limits as functions of pixel sizes. Solid lines denote the actual pixel size range of the instruments, whereas dashed lines show their extrapolation to cover the whole size range 0.375 km^2 – 9.6 km^2.

Application of the OOp-s matches the datasets (Figure 10, Figure 11): the remaining difference of 23% between the $\Xi_{pixMODIS}(P_{VIIRS})$ and $\Xi_{pixVIIRS}(P_{MODIS})$ is a result of the later overpasses of AQUA, which registers most fires around 13:00–14:00 local time, compared to 12:00–13:30 of Suomi-NPP. The absolute peak of fire intensity, however, was estimated at 14:00–15:00 from the geostationary SEVIRI retrievals (Soares et al., 2015), practically independently from the land use type. According to those calculations (see Fig.5 there), the difference between Suomi-NPP and AQUA observations corresponds to ~20% higher total FRP for MODIS AQUA (depending on actual retrieval times, the difference is within 0%–50% range), which closely matches the 23% difference between OOp-processed FRPs (this correction is applied to the scatterplots in Figure 11).

5.5. Implications for atmospheric composition assessment

A substantial fraction of fires missed by MODIS and VIIRS, either due to cloud obscuration or finite detection limit, can lead to inconsistencies in the fire retrievals. The first problem is that the satellites register more fires in centres of the swaths than at their edges. Moreover, the orbits shift every day with revisit time of 16 days. As a result, application of an atmospheric composition model with such fires as input would lead to appearing / disappearing fire detections, missing smoke plumes, and incorrectly reproduced episodes.

The second issue is more general. The atmospheric models are calibrated and evaluated against a variety of independent observations, and mean bias of predicted concentrations is one of critical parameters. Many assessments of non-anthropogenic emissions rely on inverse problem solutions (a.k.a. top-down emission inventories). Having a fraction of fires missing, the emission inversion algorithm may tend to offset the bias due to missing fires by exaggerating the emission factors for the observed ones. Such artificial increase might partly explain the factor of 3.4 between the top-down and

bottom-up approaches to PM emission from fires, as noted in earlier studies (Kaiser et al., 2012; Soares et al., 2015). Conversely, missing fires lead to distorted pollution patterns and lower correlation with observations. In the inverse problems context, lower model-measurement correlation leads to under-estimation of optimized emission fluxes (Sofiev et al., 2024).

One of possible ways to address the problem of the omission error is to construct a fire prediction model capable of assimilating the active-fire products into the model state that exists regardless of specific observations. Such a model would allow for fires in areas not observed due to clouds or below-detection-limit. The vital part of such exercise would be the FRP observation operator constructed in this paper.

6. Conclusions

Detection limits of Fire Radiative Power (FRP) products of two low-orbit satellites, MODIS and VIIRS, have been identified and related to size of the observation pixels. Two types of observation operator (OOp) for FRP retrievals have subsequently been constructed: for individual pixels of the satellite retrievals, and for gridded representation of the FRP fields. The key parameter for the pixel-level OOp is the size of the observation pixel, which solely determines the detection limit as a linear function of the pixel area, with different coefficients for day / night and MODIS / VIIRS retrievals in clear-sky conditions. For gridded representation, the fraction of the largest fire-pixel in the total grid-cell FRP and cloud cover are also important. The probability of detecting even a powerful fire can be as low as 30% for regions with a dense cloud cover. Fires can also be overshadowed by thin clouds or fire smoke attenuating the irradiance and reducing the retrieved FRP.

Application of the OOp-s confirmed their internal consistency: OOp-processed MODIS and VIIRS retrievals, with a correction to the different overpass times, showed a close match of the retrieved FRP.

The detection limits of the FRP products of MODIS Collection 6.1 are 5.7 MW / 3.7 MW for day- / night-time overpasses for the smallest-size pixels in the middle of the swath (about-half of those earlier reported for Collection 5). For VIIRS Collection 2, these are 3.7 MW and 0.7 MW, respectively. Finite detection limit leads to an omission of small fires.

The suggested formulations were developed for MODIS and VIIRS, but can also be used, with refitted coefficients, for other low-orbit and, potentially, geostationary instruments.

7. Code and data availability

Code of the observation operator and its coefficients identified for MODIS and VIIRS are available from the GitHub public repository: https://github.com/fmidev/FRP_OOp and from Zenodo archive https://doi.org/10.5281/ZENODO.18339604 (Sofiev and Kouznetsov, 2026).

8. Author contribution

MS developed the concept, performed data analysis, and wrote the paper; RK participated in the concept development, contributed to data analysis and edited the paper.

9. Competing interests

The authors declare that they have no competing interests

10. Acknowledgements

The work has been performed within the scope of H2020 EXHAUSTION (European domain, grant No 820655), FirEUrisk (sensitivity regionalization, grant No 101003890), Finnish Research Council HEATCOST (global dimension, grant No 334798) and VFSP-WASE (operational aspects, grant No 359421) projects.

The authors deeply appreciate numerous discussions within the SILAM team, which gave a lot of inspiration and ideas to consider.

11. References

Archibald, S., Roy, D.P., 2009. Identifying individual fires from satellite-derived burned area data, in: 2009 IEEE International Geoscience and Remote Sensing Symposium. Presented at the 2009 IEEE International Geoscience and Remote Sensing Symposium, IEEE, Cape Town, South Africa, p. III-160-III–163. https://doi.org/10.1109/IGARSS.2009.5417974

Arino, O., Casadio, S., Serpe, D., 2012. Global night-time fire season timing and fire count trends using the ATSR instrument series. Remote Sensing of Environment 116, 226–238. https://doi.org/10.1016/j.rse.2011.05.025

Banks, A.C., Prunet, P., Chimot, J., Pina, P., Donnadille, J., Jeansou, E., Lux, M., Petihakis, G., Korres, G., Triantafyllou, G., Fontana, C., Estournel, C., Ulses, C., Fernandez, L., 2012. A satellite ocean color observation operator system for eutrophication assessment in coastal waters. Journal of Marine Systems 94, S2–S15. https://doi.org/10.1016/j.jmarsys.2011.11.001

Bocquet, M., Elbern, H., Eskes, H., Hirtl, M., Žabkar, R., Carmichael, G.R., Flemming, J., Inness, A., Pagowski, M., Pérez Camaño, J.L., Saide, P.E., San Jose, R., Sofiev, M., Vira, J., Baklanov, A., Carnevale, C., Grell, G., Seigneur, C., 2015. Data assimilation in atmospheric chemistry models: current status and future prospects for coupled chemistry meteorology models. Atmos. Chem. Phys. 15, 5325–5358. https://doi.org/10.5194/acp-15-5325-2015

Boersma, K.F., Eskes, H.J., Dirksen, R.J., van der A, R.J., Veefkind, J.P., Stammes, P., Huijnen, V., Kleipool, Q.L., Sneep, M., Claas, J., Leitão, J., Richter, A., Zhou, Y., Brunner, D., 2011. An improved tropospheric NO₂ column retrieval algorithm for the Ozone Monitoring Instrument. Atmos. Meas. Tech. 4, 1905–1928. https://doi.org/10.5194/amt-4-1905-2011

Buchholz, R.R., Park, M., Worden, H.M., Tang, W., Edwards, D.P., Gaubert, B., Deeter, M.N., Sullivan, T., Ru, M., Chin, M., Levy, R.C., Zheng, B., Magzamen, S., 2022. New seasonal pattern of pollution emerges from changing North American wildfires. Nat Commun 13, 2043. https://doi.org/10.1038/s41467-022-29623-8

Carrassi, A., Bocquet, M., Bertino, L., Evensen, G., 2018. Data assimilation in the geosciences: An overview of methods, issues, and perspectives. WIREs Clim Change 9, e535. https://doi.org/10.1002/wcc.535

Chen, Y., Hantson, S., Andela, N., Coffield, S.R., Graff, C.A., Morton, D.C., Ott, L.E., Foufoula-Georgiou, E., Smyth, P., Goulden, M.L., Randerson, J.T., 2022. California wildfire spread derived using VIIRS satellite observations and an object-based tracking system. Sci Data 9, 249. https://doi.org/10.1038/s41597-022-01343-0

Chowdhury, S., Hänninen, R., Uppstu, A., Sofiev, M., Aunan, K., 2025. Global health burden from acute exposure to fine particles emitted by fires. npj Clean Air 1, 9pp. https://doi.org/https://doi.org/10.1038/s44407-025-00024-7

Chuvieco, E., Mouillot, F., Van Der Werf, G.R., San Miguel, J., Tanase, M., Koutsias, N., García, M., Yebra, M., Padilla, M., Gitas, I., Heil, A., Hawbaker, T.J., Giglio, L., 2019. Historical background and current developments for mapping burned area from satellite Earth observation. Remote Sensing of Environment 225, 45–64. https://doi.org/10.1016/j.rse.2019.02.013

Crutzen, P.J., Height, L.E., Krasnes, J.P., Pollock, W.H., Seiler, W., 1979. Biomass burning as a source of atmospheric gases: CO, H2, N2O, NO, CH3Cl, and COS. Nature 282, 253–256. https://doi.org/https://doi.org/10.1038/282253a0

Evans, K.F., 2007. SHDOMPPDA: A Radiative Transfer Model for Cloudy Sky Data Assimilation. Journal of the Atmospheric Sciences 64, 3854–3864. https://doi.org/10.1175/2006JAS2047.1

Freitas, S.R., Longo, K.M., Chatfield, R., Latham, D., Santos, J.C., Gielow, R., Jr, J.A.C., 2007. Including the sub-grid scale plume rise of vegetation fires in low resolution atmospheric transport models. Atmos. Chem. Phys. 7, 3385–3398. https://doi.org/https://doi.org/10.5194/acp-7-3385-2007

Giglio, L., 2024a. VIIRS/NPP Active Fires 6-Min L2 Swath 375m V002. https://doi.org/10.5067/VIIRS/VNP14IMG.002

Giglio, L., 2024b. VIIRS/JPSS1 Active Fires 6-Min L2 Swath 375m V002. https://doi.org/10.5067/VIIRS/VJ114IMG.002

Giglio, L., Justice, C., 2021a. MODIS/Terra Thermal Anomalies/Fire 5-Min L2 Swath 1km V061. https://doi.org/10.5067/MODIS/MOD14.061

Giglio, L., Justice, C., 2021b. MODIS/Aqua Thermal Anomalies/Fire 5-Min L2 Swath 1km V061. https://doi.org/10.5067/MODIS/MYD14.061

Giglio, L., Schroeder, W., Hall, J.V., Justice, C.O., 2021. MODIS Collection 6 and Collection 6.1 Active Fire Product User's Guide Version 1.0 (NASA Tech Memo). NASA.

Giglio, L., Schroeder, W., Justice, C.O., 2016. The collection 6 MODIS active fire detection algorithm and fire products. Remote Sensing of Environment 178, 31–41. https://doi.org/10.1016/j.rse.2016.02.054

Greenwald, T.J., Hertenstein, R., Vukićević, T., 2002. An All-Weather Observational Operator for Radiance Data Assimilation with Mesoscale Forecast Models. Mon. Wea. Rev. 130, 1882–1897. https://doi.org/10.1175/1520-0493(2002)130%3C1882:AAWOOF%3E2.0.CO;2

Greenwald, T.J., Vukićevic, T., Grasso, L.D., Vonder, T.H., 2004. Adjoint sensitivity analysis of an observational operator for visible and infrared cloudy-sky radiance assimilation. Q. J. R. Meteorol. Soc. 130, 685–705. https://doi.org/10.1256/qj.03.44

Ichoku, C., Kaufman, Y.J., 2005. A method to derive smoke emission rates from MODIS fire radiative energy measurements. IEEE Trans. Geosci. Remote Sensing 43, 2636–2649. https://doi.org/10.1109/TGRS.2005.857328

Kaiser, J.W., Heil, A., Andreae, M.O., Benedetti, A., Chubarova, N., Jones, L., Morcrette, J.-J., Razinger, M., Schultz, M.G., Suttie, M., van der Werf, G.R., 2012. Biomass burning emissions estimated with a global fire assimilation system based on observed fire radiative power. Biogeosciences 9, 527–554. https://doi.org/10.5194/bg-9-527-2012

Kaufman, Y.J., Justice, C.O., Flynn, L.P., Kendall, J.D., Prins, E.M., Giglio, L., Ward, D.E., Menzel, W.P., Setzer, A.W., 1998. Potential global fire monitoring from EOS-MODIS. J. Geophys. Res. 103, 32215–32238. https://doi.org/10.1029/98JD01644

Khabarov, N., Krasovskii, A., Obersteiner, M., Swart, R., Dosio, A., San-Miguel-Ayanz, J., Durrant, T., Camia, A., Migliavacca, M., 2016. Forest fires and adaptation options in Europe. Reg Environ Change 16, 21–30. https://doi.org/10.1007/s10113-014-0621-0

Kollanus, V., Prank, M., Gens, A., Soares, J., Vira, J., Kukkonen, J., Sofiev, M., Salonen, R.O., Lanki, T., 2017. Mortality due to Vegetation Fire–Originated $PM_{2.5}$ Exposure in Europe—Assessment for the Years 2005 and 2008. Environmental Health Perspectives 125, 30–37. https://doi.org/10.1289/EHP194

Kostka, P.M., Weissmann, M., Buras, R., Mayer, B., Stiller, O., 2014. Observation Operator for Visible and Near-Infrared Satellite Reflectances. Journal of Atmospheric and Oceanic Technology 31, 1216–1233. https://doi.org/10.1175/JTECH-D-13-00116.1

Li, Y., Tong, D., Ma, S., Freitas, S.R., Ahmadov, R., Sofiev, M., Zhang, X., Kondragunta, S., Kahn, R., Tang, Y., Baker, B., Campbell, P., Saylor, R., Grell, G., Li, F., 2022. Impacts of estimated plume rise on $PM_{2.5}$ exceedance prediction during extreme wildfire events: A comparison of three schemes

(Briggs, Freitas, and Sofiev) (preprint). Aerosols/Atmospheric Modelling/Troposphere/Chemistry (chemical composition and reactions). https://doi.org/10.5194/egusphere-2022-713

Li, Z., Kaufman, Y.J., Ichoku, C., Fraser, R., Trishchenko, A., Giglio, L., Jin, J.-Z., Yu, X., 2001. A review of AVHRR-based active fire detection algorithms: principles, limitations, and recommendations, in: Global and Regional Vegetation Fire Monitoring from Space: Planning a Coordinated International Effort. SPB Academic Publisher, The Hague, pp. 199–225.

Maier, S.W., Russell-Smith, J., Edwards, A.C., Yates, C., 2013. Sensitivity of the MODIS fire detection algorithm (MOD14) in the savanna region of the Northern Territory, Australia. ISPRS Journal of Photogrammetry and Remote Sensing 76, 11–16. https://doi.org/10.1016/j.isprsjprs.2012.11.005

MODIS Atmosphere Science Team, 2017a. MODIS/Aqua Cloud Mask and Spectral Test Results 5-Min L2 Swath 250m and 1km. https://doi.org/10.5067/MODIS/MYD35_L2.061

MODIS Atmosphere Science Team, 2017b. MODIS/Terra Cloud Mask and Spectral Test Results 5-Min L2 Swath 250m and 1km. https://doi.org/10.5067/MODIS/MOD35_L2.061

Nishihama, M., Wolfe, R., Solomon, D., Patt, F., Blanchette, J., Fleig, A., Masuoka, E., 1997. MODIS Level 1A Earth Location: Algorithm Theoretical Basis Document Version 3.0 (NASA Tech Memo No. SDST-092), MODIS Technical Report Series. NASA Goddard Space Flight Center, Greenbelt, MD.

Parrington, M., Whaley, C.H., French, N.H.F., Buchholz, R.R., Pan, X., Wiedinmyer, C., Hyer, E.J., Kondragunta, S., Kaiser, J.W., Di Tomaso, E., Van Der Werf, G.R., Sofiev, M., Barsanti, K.C., Da Silva, A.M., Darmenov, A.S., Tang, W., Griffin, D., Desservettaz, M., Carter, T. (Tess), Paton-Walsh, C., Liu, T., Uppstu, A., Palamarchuk, J., 2025. Biomass burning emission estimation in the MODIS era: State-of-the-art and future directions. Elem Sci Anth 13, 00089. https://doi.org/10.1525/elementa.2024.00089

Rémy, S., Veira, A., Paugam, R., Sofiev, M., Kaiser, J.W., Marenco, F., Burton, S.P., Benedetti, A., Engelen, R.J., Ferrare, R., Hair, J.W., 2017. Two global data sets of daily fire emission injection heights since 2003. Atmos. Chem. Phys. 17, 2921–2942. https://doi.org/10.5194/acp-17-2921-2017

Roberts, G.J., Wooster, M.J., 2008. Fire Detection and Fire Characterization Over Africa Using Meteosat SEVIRI. IEEE Trans. Geosci. Remote Sensing 46, 1200–1218. https://doi.org/10.1109/TGRS.2008.915751

Roy, D.P., Boschetti, L., Justice, C.O., Ju, J., 2008. The collection 5 MODIS burned area product — Global evaluation by comparison with the MODIS active fire product. Remote Sensing of Environment 112, 3690–3707. https://doi.org/10.1016/j.rse.2008.05.013

Schroeder, W., 2020a. VIIRS (S-NPP) I Band 375 m Active Fire locations NRT (Vector data). https://doi.org/10.5067/FIRMS/VIIRS/VNP14IMGT_NRT.002

Schroeder, W., 2020b. VIIRS (NOAA-20/JPSS-1) I Band 375 m Active Fire locations NRT (Vector data). https://doi.org/10.5067/FIRMS/VIIRS/VJ114IMGT_NRT.002

Schroeder, W., Csiszar, I., Morisette, J., 2007. Quantifying the impact of cloud obscuration on remote sensing of active fires in the Brazilian Amazon. Remote Sensing of Environment 112, 456 − 470. https://doi.org/10.1016/j.rse.2007.05.004

Schroeder, W., Ellicott, E., Ichoku, C., Ellison, L., Dickinson, M.B., Ottmar, R.D., Clements, C., Hall, D., Ambrosia, V., Kremens, R., 2014a. Integrated active fire retrievals and biomass burning emissions using complementary near-coincident ground, airborne and spaceborne sensor data. Remote Sensing of Environment 140, 719–730. https://doi.org/10.1016/j.rse.2013.10.010

Schroeder, W., Oliva, P., Giglio, L., Csiszar, I.A., 2014b. The New VIIRS 375 m active fire detection data product: Algorithm description and initial assessment. Remote Sensing of Environment 143, 85–96. https://doi.org/10.1016/j.rse.2013.12.008

Schroeder, W., Prins, E., Giglio, L., Csiszar, I., Schmidt, C., Morisette, J., Morton, D., 2008. Validation of GOES and MODIS active fire detection products using ASTER and ETM+ data. Remote Sensing of Environment 112, 2711–2726. https://doi.org/10.1016/j.rse.2008.01.005

Schultz, M.G., Wooster, M., Boucher, O., Doutriaux-Boucher, M., Granier, C., Heil, A., Hollingsworth, A., Kaiser, J.W., Kasikowski, T., Morcrette, J.-J., Roberts, G., Simmons, A., van der Werf, G.R., Sofiev, M., 2008. Evaluation of a Fire Radiative Power Product derived from Meteosat 8/9 and Identification of Operational User Needs (No. EUM/CO/06/4600000277/YG). EUMETSAT.

Soares, J., Sofiev, M., Hakkarainen, J., 2015. Uncertainties of wild-land fi res emission in AQMEII phase 2 case study. Atmospheric Environment 115, 361–370. https://doi.org/10.1016/j.atmosenv.2015.01.068

Sofiev, M., Ermakova, T., Vankevich, R., 2012. Evaluation of the smoke-injection height from wild-land fires using remote-sensing data. Atmospheric Chemistry and Physics 12, 1995–2006. https://doi.org/10.5194/acp-12-1995-2012

Sofiev, M., Kouznetsov, R., 2026. FRP_OOp: OOp code used for the Egusphere submission on Jan 2026. https://doi.org/10.5281/ZENODO.18339604

Sofiev, M., Palamarchuk, J., Kouznetsov, R., Abramidze, T., Adams-Groom, B., Antunes, C.M., Ariño, A.H., Bastl, M., Belmonte, J., Berger, U.E., Bonini, M., Bruffaerts, N., Buters, J., Cariñanos, P., Celenk, S., Ceriotti, V., Charalampopoulos, A., Clewlow, Y., Clot, B., Dahl, A., Damialis, A., De Linares, C., De Weger, L.A., Dirr, L., Ekebom, A., Fatahi, Y., Fernández González, M., Fernández González, D., Fernández-Rodríguez, S., Galán, C., Gedda, B., Gehrig, R., Geller Bernstein, C., Gonzalez Roldan, N., Grewling, L., Hajkova, L., Hänninen, R., Hentges, F., Jantunen, J., Kadantsev, E., Kasprzyk, I., Kloster, M., Kluska, K., Koenders, M., Laffársová, J., Leru, P.M., Lipiec, A., Louna-Korteniemi, M., Magyar, D., Majkowska-Wojciechowska, B., Mäkelä, M., Mitrovic, M., Myszkowska, D., Oliver, G., Östensson, P., Pérez-Badia, R., Piotrowska-Weryszko, K., Prank, M., Przedpelska-Wasowicz, E.M., Pätsi, S., Rajo, F.J.R., Ramfjord, H., Rapiejko, J., Rodinkova, V., Rojo, J., Ruiz-Valenzuela, L., Rybnicek, O., Saarto, A., Sauliene, I., Seliger, A.K., Severova, E., Shalaboda, V., Sikoparija, B., Siljamo, P., Soares, J., Sozinova, O., Stangel, A., Stjepanović, B., Teinemaa, E., Tyuryakov, S., Trigo, M.M., Uppstu, A., Vill, M., Vira, J., Visez, N., Vitikainen, T., Vokou, D., Weryszko-Chmielewska, E., Karppinen, A., 2024. European pollen reanalysis, 1980–2022, for alder, birch, and olive. Sci Data 11, 1082. https://doi.org/10.1038/s41597-024-03686-2

Sofiev, M., Vankevich, R., Ermakova, T., Hakkarainen, J., 2013. Global mapping of maximum emission heights and resulting vertical profiles of wildfire emissions. Atmospheric Chemistry and Physics 13, 7039–7052. https://doi.org/10.5194/acp-13-7039-2013

Sofiev, M., Vankevich, R., Lotjonen, M., Prank, M., Petukhov, V., Ermakova, T., Koskinen, J., Kukkonen, J., 2009. An operational system for the assimilation of the satellite information on wild-land fires for the needs of air quality modelling and forecasting. Atmospheric Chemistry and Physics 9, 6833–6847. https://doi.org/https://doi.org/10.5194/acp-9-6833-2009

VIIRS Calibration Support Team (VCST), 2021a. VIIRS/JPSS1 Imagery Resolution Terrain-Corrected Geolocation L1 6-Min Swath- 375m. https://doi.org/10.5067/VIIRS/VJ103IMG.021

VIIRS Calibration Support Team (VCST), 2021b. VIIRS/NPP Imagery Resolution Terrain-Corrected Geolocation L1 6-Min Swath- 375m. https://doi.org/10.5067/VIIRS/VNP03IMG.002

Vilar, L., Camia, A., San-Miguel-Ayanz, J., 2015. A comparison of remote sensing products and forest fire statistics for improving fire information in Mediterranean Europe. European Journal of Remote Sensing 48, 345–364. https://doi.org/10.5721/EuJRS20154820

Wiedinmyer, C., Akagi, S.K., Yokelson, R.J., Emmons, L.K., Al-Saadi, J.A., Orlando, J.J., Soja, A.J., 2011. The Fire INventory from NCAR (FINN): a high resolution global model to estimate the emissions from open burning. Geosci. Model Dev. 4, 625–641. https://doi.org/10.5194/gmd-4-625-2011

Wolfe, R.E., Lin, G., Nishihama, M., Tewari, K.P., Tilton, J.C., Isaacman, A.R., 2013. Suomi NPP VIIRS prelaunch and on-orbit geometric calibration and characterization. J. Geophys. Res. Atmos. 118. https://doi.org/10.1002/jgrd.50873

Xu, W., Wooster, M.J., 2023. Sentinel-3 SLSTR active fire (AF) detection and FRP daytime product - Algorithm description and global intercomparison to MODIS, VIIRS and landsat AF data. Science of Remote Sensing 7, 100087. https://doi.org/10.1016/j.srs.2023.100087

Xu, W., Wooster, M.J., Kaneko, T., He, J., Zhang, T., Fisher, D., 2017. Major advances in geostationary fire radiative power (FRP) retrieval over Asia and Australia stemming from use of Himarawi-8 AHI. Remote Sensing of Environment 193, 138–149. https://doi.org/10.1016/j.rse.2017.02.024

Zubkova, M., Humber, M.L., Giglio, L., 2023. Is global burned area declining due to cropland expansion? How much do we know based on remotely sensed data? International Journal of Remote Sensing 44, 1132–1150. https://doi.org/10.1080/01431161.2023.2174389